Journal of Quantitative Spectroscopy & Radiative Transfer 142 (2014) 25–36

Contents lists available at ScienceDirect

Journal of Quantitative Spectroscopy & Radiative Transfer

journal homepage: www.elsevier.com/locate/jqsrt

On the influence of cloud fraction diurnal cycle and sub-grid cloud optical thickness variability on all-sky direct aerosol radiative forcing

Min Min, Zhibo Zhang *

Department of Physics, University of Maryland at Baltimore County (UMBC), 1000 Hilltop Circle, Baltimore, MD 21250, USA

ARTICLE INFO

Article history:
Received 14 October 2013
Received in revised form
15 March 2014
Accepted 17 March 2014
Available online 25 March 2014

Keywords:
Above-cloud aerosol
Cloud diurnal cycle
Radiative forcing
MODIS
CALIPSO
SEVIRI

ABSTRACT

The objective of this study is to understand how cloud fraction diurnal cycle and sub-grid cloud optical thickness variability influence the all-sky direct aerosol radiative forcing (DARF). We focus on the southeast Atlantic region where transported smoke is often observed above low-level water clouds during burning seasons. We use the CALIOP observations to derive the optical properties of aerosols. We developed two diurnal cloud fraction variation models. One is based on sinusoidal fitting of MODIS observations from Terra and Aqua satellites. The other is based on high-temporal frequency diurnal cloud fraction observations from SEVIRI on board of geostationary satellite. Both models indicate a strong cloud fraction diurnal cycle over the southeast Atlantic region. Sensitivity studies indicate that using a constant cloud fraction corresponding to Aqua local equatorial crossing time (1:30 PM) generally leads to an underestimated (less positive) diurnal mean DARF even if solar diurnal variation is considered. Using cloud fraction corresponding to Terra local equatorial crossing time (10:30 AM) generally leads overestimation. The biases are a typically around 10–20%, but up to more than 50%.

The influence of sub-grid cloud optical thickness variability on DARF is studied utilizing the cloud optical thickness histogram available in MODIS Level-3 daily data. Similar to previous studies, we found the above-cloud smoke in the southeast Atlantic region has a strong warming effect at the top of the atmosphere. However, because of the plane-parallel albedo bias the warming effect of above-cloud smoke could be significantly overestimated if the grid-mean, instead of the full histogram, of cloud optical thickness is used in the computation. This bias generally increases with increasing above-cloud aerosol optical thickness and sub-grid cloud optical thickness inhomogeneity. Our results suggest that the cloud diurnal cycle and sub-grid cloud variability are important factors to be accounted for in the studies of all-sky DARF.

1. Introduction

Over the last decade, significant advances have been made in quantifying the direct aerosol radiative forcing (DARF) under clear-sky (i.e., cloud-free) conditions based on satellite remote sensing observations [1] and model simulations [2]. In contrast, DARF under cloudy conditions remain poorly understood [2]. One of the important reasons for this is because conventional satellite-based remote sensing methods, in particular those based on passive sensors, can provide aerosol property retrievals only under cloud-free conditions. As a result, there has been a lack of observational constraints on model simulations of cloudy-sky DARF. Recently, the global observations

* Corresponding author.
E-mail address: Zhibo.Zhang@umbc.edu (Z. Zhang).

http://dx.doi.org/10.1016/j.jqsrt.2014.03.014

from the space-born lidar Cloud-Aerosol Lidar with Orthogonal Polarization (CALIOP) onboard of the Cloud-Aerosol Lidar and Infrared Pathfinder Satellite Observations (CALIPSO) mission have greatly improved our knowledge of the vertical distribution of aerosols and clouds, in particular the occurrence of above-cloud aerosols (ACA), and thus has opened a new avenue for studying the cloudy-sky DARF [3–5]. In addition to CALIOP observation, attempts have also been made recently to detect ACAs and retrieve their properties using passive imagers. Waquet et al. [6] developed a method based on multi-angular, polarization measurements from Polarization and Directionality of the Earth Reflectances (POLDER) to retrieve the aerosol optical thickness (AOT) of above-cloud smoke. This method has recently been extended to include both smoke and dust aerosols [7]. Most recently, Torres et al. [8] developed an algorithm to retrieve the AOT of ACA using Ozone Monitoring Instrument (OMI) on board of Aura satellite. Jethva et al. [9] demonstrated a color ratio method to retrieve the above-cloud AOT based on MODIS multiple spectral cloud reflectance measurements. A review of the emerging satellite-based observations of ACA can be found in Yu and Zhang [10]. These novel techniques based on passive sensors will provide a revealing perspective on ACA complementary to CALIOP. In particular, the global above-cloud aerosol retrievals from POLDER [11] will soon become publically available (Waquet 2013, personal communication). These new datasets will provide us more opportunities for comparison and evaluation studies like [12] to understand the accuracy and limitations of each method.

Using multiple years of CALIOP observations, Devasthale and Thomas [4] located several geographical regions where elevated aerosols are often found above low-level liquid phase clouds. For example, during the austral winter and spring light-absorbing smoke aerosols originating from seasonal burning of the southwestern African Savannah are often observed over the bright stratocumulus decks over southeast Atlantic. In contrast to cloud-free DARF that generally has a cooling effect at the top of the atmosphere (TOA), above-cloud smoke can have a strong warming effect at TOA because the bright cloud layer beneath significantly enhances smoke absorption [13–15]. In addition to DARF, above-cloud aerosols can also have semi-direct effects on the clouds beneath [16,17]. For these reasons, above-cloud smoke in the southeast Atlantic has attracted increasing attention recently.

The CALIOP ACA property retrievals have been used in several recent studies in combination with cloud products from Moderate Resolution Imaging Spectroradiometer (MODIS) to derive the DARF of above-cloud light-absorbing aerosols in southeast Atlantic region with radiative transfer simulations [15,18,19]. In Chand et al. [15], the CALIOP level-2 above-cloud AOT retrievals [20] and the MODIS monthly mean cloud optical thickness (COT) from the MODIS monthly level-3 product ($1^\circ \times 1^\circ$ resolution) were both aggregated to $5^\circ \times 5^\circ$ resolution and then used to compute the DARF of above-cloud smoke. A major point made in this study is that the all-sky TOA DARF is strongly modulated by the underlying cloud fraction as a result of the dramatic difference between the clear-sky DARF (generally negative) and the DARF of ACA (strongly positive). Based on a similar methodology as in Chand et al. [15], Oikawa et al. [18] used the MODIS level-3 monthly mean COT and aggregated CALIOP ACA retrievals to derive the all-sky DARF and compared the results with model simulations from a GCM. These recent studies have shed light on the important and unique role of ACA in the climate system and clearly demonstrated the usefulness of satellite remote sensing data; in particular, CALIOP data, for estimating ACA DARF. However, these studies have a common limitation in that they use coarse resolution monthly mean data in their computation, which obscures the influence of cloud diurnal cycle and sub-grid spatial variability on all-sky DARF.

It is well known that marine boundary layer (MBL) clouds, such as those over southeast Atlantic, have a strong diurnal cycle driven largely by cloud solar absorption [21–23]. Wood et al. [22] found that the diurnal amplitudes of the liquid water path (LWP) in low cloud regions to the west of continents (e.g., southeast Atlantic and southeast Pacific stratocumulus decks) are typically 15–35% fraction of the diurnal mean. In this study, we developed two diurnal cloud fraction variation models (see Section 3 for details). One is based on sinusoidal fitting of MODIS observations from Terra (10:30 AM local equatorial crossing time) and Aqua (1:30 PM local equatorial crossing time) satellites. The other is based on high-temporal frequency diurnal cloud fraction observations from SEVIRI (Spinning Enhanced Visible and Infrared Imager) on board of geostationary satellite. Both models indicate a strong cloud fraction diurnal cycle over the southeast Atlantic region. In both Chand et al. [15] and Oikawa et al. [18], as well as most previous studies [5,19,24], the cloud property used in ACA DARF computations were from retrievals based on polar-orbiting satellites (e.g., Terra or Aqua MODIS), which provide only an instantaneous snapshot of the cloud field at the local crossing time. As a result, the strong diurnal cycle of MBL clouds is not accounted for in these studies, which as shown later in this study could cause significant bias in diurnal mean DARF computation. MBL clouds are also known to have significant small-scale heterogeneity [25–27]. It is well known that using the grid mean COT to estimate the shortwave radiative effects of clouds with horizontal heterogeneity can lead to significant bias, an effect known as the “plane-parallel albedo bias” [27–29]. Note that several of the above-motioned studies have used the coarse resolution grid-mean COT in ACA DARF computation (e.g., $5^\circ \times 5^\circ$ resolution as in Chand et al. [15]). The potential impact of plane-parallel albedo bias on these studies remains unknown.

The objective of the present investigation is to study the influence of the temporal (i.e., diurnal cycle) and spatial variability (i.e., sub-grid heterogeneity) of clouds on the estimate of all-sky ACA DARF. Here we will focus on the southeast Atlantic region where light-absorbing aerosols are often found above low-level MBL clouds. We will first briefly introduce the CALIOP, MODIS and SEVIRI products used in this study in Section 2. In Section 3, we present a study of how cloud fraction diurnal cycle influences the all-sky ACA DARF computation. In Section 4, we present a study of how sub-grid heterogeneity

influences the ACA DARF computation, followed by conclusions and discussions in Section 5.

2. MODIS, CALIOP and SEVIRI data

In this study we focus on the southeast Atlantic region bounded within [10°W-15°E longitude; 20°S-0°S latitude]. Previous studies found high occurrence frequency of above-cloud light-absorbing smoke in this region during burning seasons (July, August, and September) [4,13,14,17]. We use MODIS and SEVERI observations to derive the cloud fraction diurnal variations over this region. We use CALIOP operational aerosol layer products for the needed aerosol properties in DARF computation.

We use the Collection 5.1 level-3 daily cloud products (MOD08_D3 from Terra and MYD08_D3 from Aqua) at $1^\circ \times 1^\circ$ resolution [30] from the two MODIS instruments onboard Terra and Aqua satellites respectively. Terra has a nominal ascending node equatorial crossing time of 10:30 AM local time. Aqua's local equatorial crossing time is 01:30 PM. As demonstrated in previous studies e.g., [31–34], because of this crossing time difference, cloud property differences between Terra-MODIS and Aqua-MODIS provide useful information for studying cloud diurnal cycle. A particular useful cloud product in MODIS level-3 product is the joint histogram of COT vs. cloud top pressure (CTP) (hereafter "COT–CTP joint histogram"). It is derived using daily counts of successful level-2 pixel retrievals that fall into each joint COT–CTP bin. Eleven COT bins, ranging from 0 to 100, and 13 CTP bins, ranging from 200 to 1000 mb, comprise the histogram. Recently, Zhang et al. [35] developed a novel method for computing the ACA DARF using MODIS and CALIOP data, in which they use the aerosol layer height information from CALIOP to identify the population of below-aerosol clouds in MODIS COT–CTP joint histogram and to derive the corresponding COT histogram for ACA DARF computation. We adopt this approach in this study to derive the below-aerosol COT from MODIS level-3 daily COT–CTP joint histogram. It should be noted that because the joint histogram contains eleven COT bins ranging from 0 to 100 it provides rich information on sub-grid cloud variability. Previous studies have used this information to study, for example, the plane-parallel albedo bias [28].

We also use SEVIRI products from Satellite Application Facility on Climate Monitoring (CM-SAF) of the European Organization for the Exploitation of Meteorological Satellites (EUMETSAT) as an independent data source to derive cloud fraction diurnal variation. SEVIRI is a 12-channel imager on board of the Meteosat Second Generation (MSG) geostationary satellite operated by EUMETSAT. An overview of the SEVIRI cloud property products and retrieval algorithm can be found in [36,37]. The advantage of SEVIRI cloud observation is its high temporal frequency. It observes the full disk of the Earth with an unprecedented repeat cycle of 15 min, with the southeast Atlantic region at the center of the disk.

An overview of CALIOP data processing system and retrieval products can be found in [38]. In this study, we use the level-2 5 km (horizontal resolution) CALIOP cloud and aerosol layer products [38] for above cloud aerosol detection. The detection scheme is as follows: (1) for each 5 km CALIOP profile that falls within a given latitude–longitude grid box, we first check whether there is any aerosol layer present in the profile; (2) if an aerosol layer is present we then proceed to check for the presence of an underlying liquid-phase cloud layer within the profile using the CALIOP cloud layer product; (3) if a cloud layer is also present, the profile is identified as an ACA case. The AOT of the above-cloud aerosol layer is recorded to derive the grid mean AOT for the grid box. The bottom height of the aerosol layer is also recorded to derive the grid mean aerosol layer bottom height that will be later used to determine the below-aerosol cloud population using the MODIS COT–CTP joint histogram as mentioned above.

Using the above method, we have processed MODIS and CALIOP data for the burning seasons (July–September) from year 2006 to 2012. Fig. 1 (left panel) shows a regional

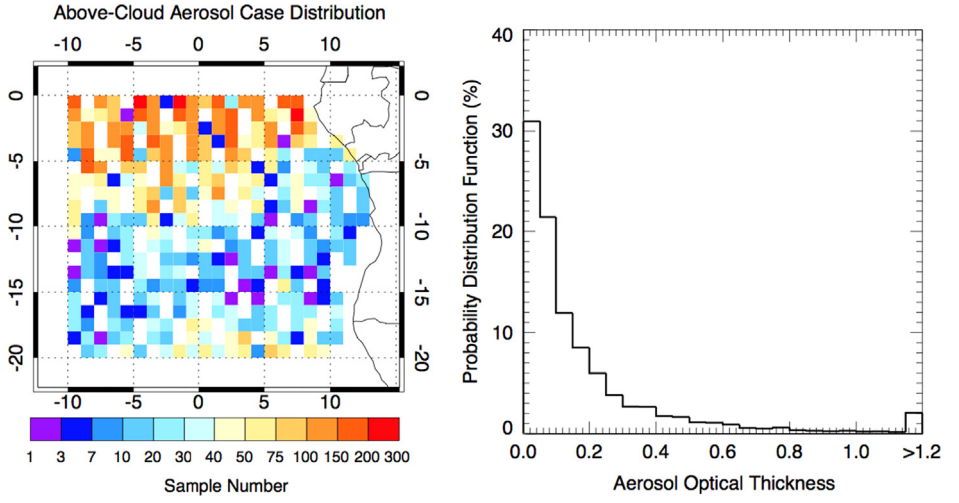

Fig. 1. (Left panel) Number of ACA per $1^\circ \times 1^\circ$ box observed by CALIOP during the burning seasons (July–September) of the year 2006–2012. (Right panel) Probability distribution function (0.05 resolution) of above-cloud aerosol optical thickness (at 532 nm) retrieved from CALIPSO level 2 aerosol layer product based on the above-cloud aerosol samples in the left panel.

map of the total number of ACA cases (each case is a 5 km CALIOP profile) per $1^\circ \times 1^\circ$ grid box detected by CALIOP over the 7 years we processed. Fig. 1 (right panel) shows the probability distribution function (PDF) of above-cloud 532 nm AOT derived from all the ACA cases in Fig. 1. Similar to previous studies [5], we found that the PDF of above-cloud AOT peaks at small values around 0.05 and then decreases with increasing AOT. We found that more than 95% of ACA cases have AOT at 532 nm lower than 0.50.

It is worth mentioning here that a recent inter-comparison of CALIOP above-cloud AOT with collocated retrievals based on POLDER and MODIS methods suggests that CALIOP tends to underestimate the above-cloud AOT [12]. In align with [12], Waquet et al. [11] found the above cloud AOT in the same southeast Atlantic region in Fig. 1 is substantially larger than the value in Fig. 1. In addition to this potential bias, CALIOP operational algorithm also often misses faint aerosol layers with AOT <0.02 at 532 nm and tends underestimate above-cloud AOT according to recent studies based on air-borne High Spectral Resolution Lidar (HRSL) [39,40]. Furthermore, it is also found that the AOT retrieved based on daytime CALIOP observation is significantly different from nighttime retrieval, which suggests calibration issues related to solar background noise e.g., [5]. As explained in Kacenelenbogen et al. [39], the underestimation of AOT by CALIOP is a result of several factors, including calibration, low signal-to-noise ratio, false and miss detection of aerosol layer, and erroneous aerosol classification (e.g., erroneous lidar ratio). In addition to AOT uncertainty, there is also large uncertainty in aerosol absorption. Based on in situ and AERONET observations made during the SAFARI 2000 campaign, Leahy et al. [41] found the single-scattering albedo (at 550 nm) of smoke over the South African region to vary from about 0.8 to 0.9, with the probability density function peak at about 0.85. Similar range of variability is also reported in Eck et al. [42]. Substantial efforts are needed to narrow down this uncertainty in aerosol absorption, as it plays a critical role determining the magnitude and even sign of the DARF.

Note that the abovementioned CALIOP AOT retrieval uncertainties are beyond the scope of this study. Interested readers are referred to the abovementioned studies, as well as Winker et al. [38] and Young et al. [43] for more detailed analysis of the uncertainties in CALIOP operational aerosol retrieval algorithm. Nevertheless, these studies suggest that the CALIOP operational retrieval is likely to underestimate the true above-cloud AOT for various reasons. We have carried out several sensitivity tests to investigate the impact of the uncertainty in AOT, as well as aerosol absorption, on our results, which will be shown along with control test based on the operational CALIOP retrieval in the following sections.

3. Influence of cloud fraction diurnal cycle on all-sky DARF

In this part, we will use two simple sensitivity studies, constrained by satellite observations, to illustrate the influence of cloud fraction diurnal cycle on estimating all-sky DARF. Here, we assume that a grid box has a time-dependent cloud fraction $f_c(t)$ and a smoke layer above the cloud. For simplicity, we assume that the AOT (τ_a) and COT (τ_c) are constant with time. Under these assumptions, the diurnal mean all-sky shortwave DARF ($\overline{F^{SW}_{all-sky}}$) for this grid box is given by

$$\overline{F^{SW}_{all-sky}} = \frac{1}{T_{total}} \int_{T_{sunrise}}^{T_{sunset}} f_c(t) F^{SW}_{cloudy}[\theta_0(t), \tau_a, \tau_c] + [1 - f_c(t)] F^{SW}_{clear}[\theta_0(t), \tau_a]\, dt, \quad (1)$$

where T_{total} is the total time in a day depending on the unit of t; $T_{sunrise}$ and T_{sunset} are the sunrise and sunset time; F^{SW}_{cloudy} is the instantaneous ACA DARF which is a function of τ_a, τ_c, and solar zenith angle $\theta_0(t)$; F^{SW}_{clear} is the instantaneous clear-sky DARF which is a function of τ_a and $\theta_0(t)$.

In the first sensitivity test, following previous studies [22,23] we use a simple sinusoidal model, constrained by the observation from Terra and Aqua MODIS, to approximate the diurnal variation of $f_c(t)$, i.e.

$$f_c(t) = A\sin[\pi(t+\phi)/12] + B, \quad (2)$$

where t is local time (h). The parameters A, ϕ, and B are, respectively, amplitude, initial phase, and diurnal mean value of cloud fraction. We can only deduce two of these parameters from the Terra and Aqua cloud fraction observations and have to assume the other one. Here, we assume that the sinusoidal cloud fraction peaks at 6:50 AM local time in the southeast Atlantic region, which is chosen based on the SEVIRI observation (see Fig. 4). This corresponds to a $\phi = -0.96$ in Eq. (2). Under this assumption, we can then solve Eq. (2) by substituting the multiple year seasonal and regional mean liquid-phase cloud fractions from Terra (f_c(10:30 AM) = 0.58) and Aqua (f_c(01:30 PM) = 0.46) MODIS to obtain $A = 0.13$ and $B = 0.51$. Fig. 2 shows the fitted sinusoidal diurnal cloud fraction and solar zenith angle cycle. We mark in the figure the Terra and Aqua local equatorial crossing times, as well as the sunrise and sunset time corresponding to the center of the interested region on the date of Aug. 15th. The fitted cloud fraction diurnal cycle reaches the maximum value of 0.63 in early morning. After sunrise, some clouds begin to dissipate as a result of increasing solar heating. At Terra crossing time, the

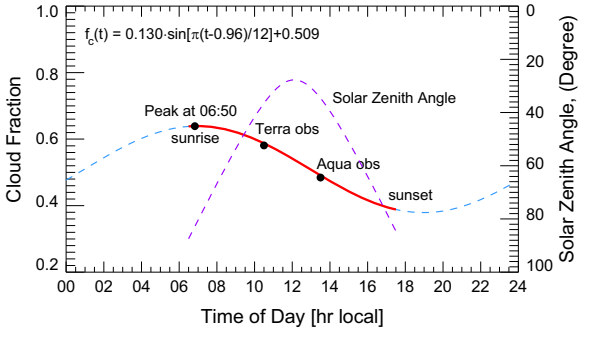

Fig. 2. A sinusoidal model to represent the diurnal variation of cloud fraction. Model parameters are determined based on the mean cloud fractions observed by Terra (10:30 AM local crossing time) and Aqua MODIS (01:30 PM local crossing time), under the assumption that the cloud fraction peaks at the local time 03:36 AM. Dashed purple line represents solar zenith angle diurnal variation. (For interpretation of the references to color in this figure legend, the reader is referred to the web version of this article.)

cloud fraction is about 0.58. The value reduces to 0.49 when Aqua crosses the equator and reaches the minimum value of 0.38 around sunset before it increases again during the nighttime.

As Eq. (1) suggests, all sky DARF $\overline{F^{SW}_{all-sky}}$ depends on incident solar condition and cloud fraction, both are functions of solar zenith angle. While the variation of solar condition has been considered in most previous studies of aerosol direct radiative forcing e.g., [16], influence of diurnally varying cloud fraction remains largely unexplored. It is also important to note that using instantaneous cloud fraction from a single MODIS instrument could lead to significant bias in computing the $\overline{F^{SW}_{all-sky}}$ even if the diurnal variation of solar zenith angle is considered. In order to understand the influence of $f_c(t)$ on $\overline{F^{SW}_{all-sky}}$ we carried out a sensitivity study shown in Fig. 3. Based on the sinusoidal cloud fraction model fitted from Terra and Aqua observations in Fig. 2, we computed the diurnal variation of all-sky shortwave DARF based on Eq. (1) for different AOT ($\tau_a = 0.05$, 0.2 and 0.5 at 550 nm). In the computation, we assumed the single scattering albedo of smoke to be 0.85 at 550 nm on the basis of the update synthesis of remote and in situ observations during the South African Regional Science Initiation 2000 [41]. Similar values for single scattering albedo of smoke have also been used in previous studies [15]. The spectral dependence of the smoke scattering properties is based on the model developed in [44]. Cloud optical thickness and effective radius are assumed to be 9.1 [45] and 10 μm, respectively. The radiative transfer computation is carried out using the RRTM_SW model [46,47]. See Table 1 for detailed information on the setup of the radiative transfer simulations.

The simulated diurnal variations of $F^{SW}_{all-sky}$ under different AOTs are shown in Fig. 3. It is interesting to note that the $F^{SW}_{all-sky}$ based on sinusoidal $f_c(t)$ (curves with solid circles) has a rather complicated diurnal variation that is different from either solar zenith variation or the sinusoidal cloud fraction diurnal cycle. For the case with $\tau_a = 0.5$ at 550 nm, the $F^{SW}_{all-sky}$ reaches its maximum value of about 30 W m^{-2} at around 09:00 AM, instead of the local noontime. The result suggests that both solar zenith angle and cloud fraction play a significant role and the diurnal variation of $F^{SW}_{all-sky}$ reflects the convolution of the two effects. In addition to the diurnal mean $F^{SW}_{all-sky}$ based on the sinusoidal $f_c(t)$ (referred to as $F^{SW}_{all-sky}(f_c(t))$ hereafter), we also computed two other sets of diurnal mean $F^{SW}_{all-sky}$ assuming constant cloud fraction throughout the day, one based on a fixed cloud fraction observation from Terra MODIS $f_c^{Terra} = 0.581$ (hereafter $F^{SW}_{all-sky}(f_c^{Terra})$) and the other based on Aqua $f_c^{Aqua} = 0.485$ (hereafter $F^{SW}_{all-sky}(f_c^{Aqua})$). When constant cloud fraction is used, the diurnal variation of $F^{SW}_{all-sky}(f_c^{Terra})$ and $F^{SW}_{all-sky}(f_c^{Aqua})$ is primarily dependent on the variation of solar zenith angle, with maximum values located around local noontime. It is worth noting that the $F^{SW}_{all-sky}(f_c^{Terra})$ seems to be biased high, while the $F^{SW}_{all-sky}(f_c^{Aqua})$ seems to be biased low, in comparison with the $F^{SW}_{all-sky}(f_c(t))$. The diurnal mean values of $F^{SW}_{all-sky}(f_c(t))$, $F^{SW}_{all-sky}(f_c^{Aqua})$ and $F^{SW}_{all-sky}(f_c^{Terra})$ under different AOTs are listed in Table 2. For the case with $\tau_a = 0.5$ at 550 nm, the $\overline{F^{SW}_{all-sky}(f_c^{Aqua})}$ is 7.0 W m^{-2}, about 16% smaller than of the $\overline{F^{SW}_{all-sky}(f_c(t))}$ (8.38 W m^{-2}). The $\overline{F^{SW}_{all-sky}(f_c^{Terra})}$ is 9.9 W m^{-2}, about 18% higher than the $\overline{F^{SW}_{all-sky}(f_c(t))}$. Similar relative differences between constant cloud fraction result and sinusoidal model are also observed for the $\tau_a = 0.05$ and 0.2 cases.

As aforementioned, there is substantial uncertainty associated with the aerosol absorption. We performed two additional tests to investigate the impact of this uncertainty on our results, as well as its relative importance with respect to cloud diurnal cycle. In one test, we increased the aerosol absorption by reducing the single-scattering albedo of the aerosol and in the other test we

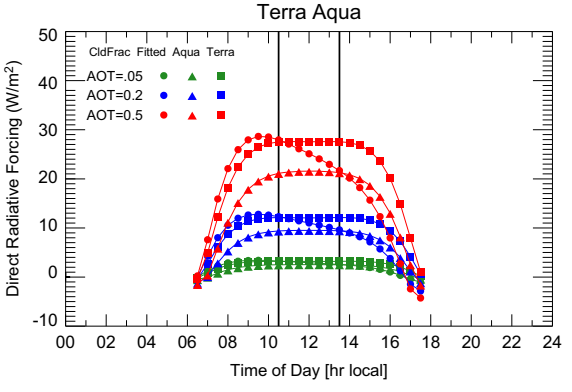

Fig. 3. Simulated diurnal variations of all-sky DARFs under different above-cloud AOTs (at 532 nm) and based on different assumptions of cloud fraction diurnal cycle. Green: AOT=0.05; blue: AOT=0.2; and red: AOT=0.5. Solid circles: all-sky DARF based on the sinusoidal model in Fig. 2; triangles: all-sky DARF under the assumption that cloud fraction is a constant throughout the day and Aqua cloud fraction observation is used; squares: all-sky DARF under the assumption that cloud fraction is a constant throughout the day and Terra cloud fraction observation is used. Vertical lines correspond to Terra and Aqua local crossing times. (For interpretation of the references to color in this figure legend, the reader is referred to the web version of this article.)

Table 1
Configurations of the RRTM-SW model.

Parameter	Values used in model
Cloud	
Phase	Liquid
Height	3–4 km
Optical thickness	9.10
Effective radius	10 μm
Above-cloud aerosol	
Type	Smoke[a]
Height	4–6 km
Single scattering albedo	0.85 (550 nm)
Other	
Atmospheric profile	tropical model
Surface albedo (Lambert)	0.05

[a] The spectral dependence of the optical properties of smoke used in this study is based on the model developed in Molineaux et al. [44].

Table 2
Summaries of simulated daily mean DARFs (W m^{-2}) and differences.

AOT (532 nm)	Sinusoidal f_c	Constant f_c (Aqua)	Difference (Aqua-f_c)	Constant f_c (Terra)	Difference (Terra-f_c)
0.05	1.00	0.84	−0.17 (−16.50%)	1.20	0.20 (19.69%)
0.20	3.76	3.15	−0.61 (−16.25%)	4.48	0.72 (19.14%)
0.50	8.38	7.03	−1.35 (−16.10%)	9.92	1.55 (18.44%)

Table 3
Same as Table 2, except that above-cloud aerosol is more absorptive in this test (the single scattering albedo at 550 nm in this test is 0.80).

AOT (532 nm)	Sinusoidal f_c	Constant f_c (Aqua)	Difference (Aqua-f_c)	Constant f_c (Terra)	Difference (Terra-f_c)
0.05	1.72	1.52	−0.20 (−11.69%)	1.96	0.24 (13.74%)
0.20	6.26	5.53	−0.73 (−11.68%)	7.11	0.85 (13.54%)
0.50	13.44	11.86	−1.58 (−11.72%)	15.21	1.78 (13.26%)

Table 4
Same as Table 2, except that above-cloud aerosol is less absorptive in this test (the single scattering albedo at 550 nm in this test is 0.90).

AOT (532 nm)	Sinusoidal f_c	Constant f_c (Aqua)	Difference (Aqua-f_c)	Constant f_c (Terra)	Difference (Terra-f_c)
0.05	0.27	0.15	−0.13 (−47.13%)	0.43	0.16 (57.60%)
0.20	1.11	0.63	−0.48 (−43.56%)	1.70	0.58 (52.49%)
0.50	2.71	1.61	−1.10 (−40.52%)	3.99	1.28 (47.35%)

reduced the aerosol absorption. The results from the two tests are shown in Tables 3 and 4. As expected, aerosol absorption has a strong impact on DARF. For example, in the AOT=0.5 case, $F^{SW}_{all-sky}(f_c(t))$ increases from 8.4 W m^{-2} to 13.4 W m^{-2} when single scattering albedo (at 550 nm) is reduced from 0.85 to 0.80. In comparison, the uncertainty associated with cloud fraction diurnal cycle is about 1.6 W m^{-2}. These tests indicate that the uncertainty caused by assuming constant cloud fraction is significant when comparing to the uncertainty associated with aerosol absorption, further attesting its importance in all-sky DARF. It is interesting to note that the impact of cloud diurnal cycle becomes even stronger when aerosol is less absorptive (see Table 4). The bias caused by using a constant cloud fraction in diurnal mean DARF computation approaches about 50%. It is probably because the magnitude of the DARF of ACA is comparable to that of clear-sky DARF when aerosol is less absorptive although the former is positive and the latter is negative. In such case the delicate balance between the two is strongly modulated by cloud fraction, which explains why a constant cloud fraction can lead substantial error in such situation.

In the second test, we use the SEVIRI CM-SAF products as an independent data source to derive cloud fraction diurnal cycle and investigate the corresponding impact on DARF. Another motivation of using SEVIRI data is to check whether DARF result based the simple sinusoidal model is in good agreement with that based on SEVIRI observation. Fig. 4 shows the diurnal variation of total cloud fraction over the southeast Atlantic region (domain average) in Fig. 1 derived from 5 years (2008–2012) of SEVIRI CM-SAF cloud products. One may note that the cloud fraction from SEVIRI in Fig. 4 is significantly higher than that from MODIS in Fig. 2, while the diurnal cycle is weaker. One reason is that SEVIRI total cloud fraction diurnal variation product does not distinguish between low and high clouds, while in Fig. 2 we only include the low-level liquid-phase clouds from MODIS. It is known that diurnal variation of convection activity over ocean and associated high clouds usually have an opposite phase than low-clouds, which diminishes the low-cloud diurnal cycle [see Fig. 4 of 23]. Even so, a significant cloud fraction diurnal cycle is still evident in Fig. 4, although month-to-month variations are large. The cloud fraction usually peaks around 7 AM in the morning and then decreases to the minimum value at around

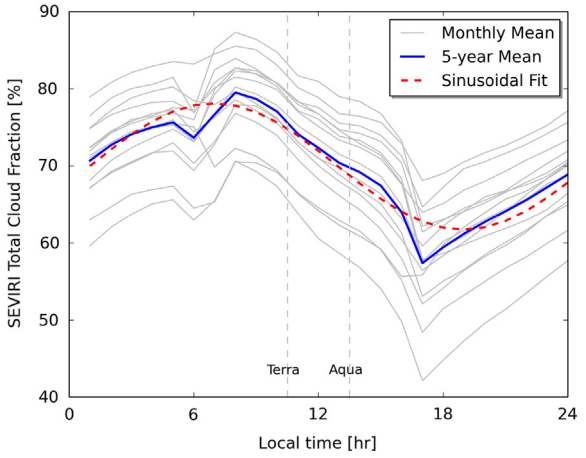

Fig. 4. Diurnal cloud fraction variation over the southeast Atlantic region derived from 5-years (2008–2012) of SEVIRI product. The gray lines correspond to monthly mean diurnal cloud fraction variation for July, August and September of each year. The solid blue line is the 5-year mean diurnal cloud fraction variation based on monthly mean results. The red dashed line corresponds to the sinusoidal fit to the 5-year mean. The two vertical dashed lines indicate the Terra and Aqua local equatorial crossing times. (For interpretation of the references to color in this figure legend, the reader is referred to the web version of this article.)

Table 5
Same as Table 2, except based on SEVIRI observations.

AOT (532 nm)	SEVIRI	Sinusoidal	Difference (Sinusoidal-SEVIRI)	Constant f_c (Aqua)	Difference (Aqua-f_c)	Constant f_c (Terra)	Difference (Terra-f_c)
0.05	1.70	1.69	−0.01 (−0.6%)	1.60	−0.09 (−5.31%)	1.83	0.14 (8.28%)
0.20	6.31	6.28	−0.04 (−0.60%)	5.95	−0.33 (−5.29%)	6.79	0.51 (8.13%)
0.50	13.96	13.84	−0.12 (−0.86%)	13.10	−0.73 (−5.30%)	14.93	1.10 (7.93%)

5 PM in the afternoon. A sinusoidal fit (red dashed line) to the 5-year mean cloud fraction cycle (solid blue line) gives $f_c(t) = 0.08sin[\pi(t - 0.96)/12] + 0.70$. Notably, the diurnal mean value is significantly larger than MODIS result in Fig. 2 and the cloud diurnal cycle is significantly weaker for the reasons mentioned above. The diurnal mean DARF computations based on 5-year mean SEVIRI observation and the sinusoidal fit are listed in Table 5. Evidently, the two are in close agreement with maximum difference smaller than 1%. The results indicate that the sinusoidal model provides an excellent approximate to the real cloud fraction diurnal cycle for DARF computation. We also computed two additional DARF, shown in Table 5, using constant cloud fractions corresponding to Terra and Aqua equatorial crossing time, respectively. Similar to what we found in the test based on MODIS observations, using a constant cloud fraction at 1:30 PM (i.e., Aqua local equatorial crossing time) leads to underestimation of diurnal mean DARF, while using cloud fraction at 10: 30 AM would lead to overestimation. The magnitude of the biases is, however, significantly smaller than that based on MODIS observations. As aforementioned, this is probably because the SEVIRI cloud diurnal cycle product does not distinguish between low and high cloud, leading to a smaller diurnal cloud fraction variation.

The sensitivity tests indicate that cloud fraction diurnal cycle is an important factor in determining the diurnal mean all-sky shortwave DARF. This is not surprising considering the strong dependence of the shortwave DARF on underlying surface reflectivity [15]. The results also indicate that using the instantaneous cloud fraction observation from a single MODIS instrument to compute the diurnal DARF may lead to systematic bias, even if the diurnal variation of solar zenith angle is considered. Finally, we would like to point out that besides cloud fraction the diurnal variation of $F^{SW}_{all-sky}$ is also dependent on several other factors, especially the diurnal variation of cloud optical thickness. In the above sensitivity study, we have assumed a constant COT = 9.1. The effect of diurnal variability on COT and thus on $F^{SW}_{all-sky}$ will need to be studied in future research.

4. Influence of sub-grid cloud spatial variability on cloudy-sky DARF

In this part, we will investigate the impact of sub-grid scale horizontal variability of COT on estimating cloudy-sky DARF due to ACA. It follows from Eq. (1) that the corresponding impact on all-sky DARF is simply scaled by cloud fraction. MBL clouds are known to have a significant small-scale horizontal variability [25,26]. Because of the nonlinear dependence of cloud reflectance on COT, if the COT in a grid box has significant horizontal variability, the grid-mean cloud reflectance computed based on grid mean optical thickness $R(\langle\tau\rangle)$ is biased high in comparison with the computation considering sub-grid COT variation ($\langle R\rangle$):

$$R(\langle\tau_c\rangle) = R\left(\int_0^\infty \tau_c p(\tau_c)\, d\tau_c\right) \geq \langle R\rangle = \int_0^\infty R(\tau_c) p(\tau_c)\, d\tau_c \quad (3)$$

where $p(\tau_c)$ is the probability density function of COT within the grid. This is the well-known plane-parallel albedo bias [28,48,49].

Including an aerosol layer above cloud significantly complicates the problem. By definition, the TOA shortwave DARF of ACA is the difference of the TOA shortwave reflectance between clouds without and with above-cloud aerosols:

$$F^{SW}_{cloudy} = R^{SW}_{cloud} - R^{SW}_{cloud+ACA}. \quad (4)$$

Consider a grid box with significant horizontal variation of COT but a constant AOT. The grid mean cloudy-sky TOA DARF is given by

$$\langle F^{SW}_{cloudy}\rangle = \langle R^{SW}_{cloud}\rangle - \langle R^{SW}_{cloud+ACA}\rangle, \quad (5)$$

where $\langle R^{SW}_{cloud}\rangle = \int_0^\infty R^{SW}_{cloud}(\tau_c) p(\tau_c)\, d\tau_c$ and $\langle R^{SW}_{cloud+ACA}\rangle = \int_0^\infty R^{SW}_{cloud+ACA}(\tau_a, \tau_c) p(\tau_c)\, d\tau_c$. As in previous studies e.g., [15,18], the grid mean DARF could also be estimated based on the grid mean COT:

$$F^{SW}_{cloudy}(\tau_a, \langle\tau_c\rangle) = R^{SW}_{cloud}(\tau_a, \langle\tau_c\rangle) - R^{SW}_{cloud+ACA}(\tau_a, \langle\tau_c\rangle), \quad (6)$$

where $\langle\tau_c\rangle = \int_0^\infty \tau_c p(\tau_c)\, d\tau_c$ is the grid mean COT. The difference between the two methods is

$$F^{SW}_{cloudy}(\langle\tau_c\rangle) - \langle F^{SW}_{cloudy}\rangle = [R^{SW}_{cloud}(\langle\tau_c\rangle) - \langle R^{SW}_{cloud}\rangle] - [R^{SW}_{cloud+ACA}(\langle\tau_c\rangle) - \langle R^{SW}_{cloud+ACA}\rangle], \quad (7)$$

The sign of $F^{SW}_{cloudy}(\langle\tau_c\rangle) - \langle F^{SW}_{cloudy}\rangle$ is determined by the difference between the two terms in the brackets on right hand side of Eq. (7). Although both terms are expected to be positive on the basis of Eq. (3), their difference is less certain and could be dependent on the properties of both cloud and above-cloud aerosol. Nevertheless, we argue that in the case of light-absorbing smoke above cloud $F^{SW}_{cloudy}(\langle\tau_c\rangle) - \langle F^{SW}_{cloudy}\rangle$ is likely to be positive. When the AOT of ACA is small, the $R^{SW}_{cloud+ACA}(\tau_a, \tau_c)$ can be roughly approximated by

$$R^{SW}_{cloud+ACA}(\tau_a, \tau_c) \approx R^{SW}_{cloud}(\tau_c) T^2(\tau_a) + R^{SW}_{ACA}(\tau_a). \quad (8)$$

In the above equation, $T^2(\tau_a)$ is the direct two-way transmittance of the ACA layer. The term $R^{SW}_{ACA}(\tau_a)$ is the reflection of the ACA layer, which is not affected by cloud variability. Note that the dependence on solar angle has been dropped in the equation. Substituting Eq. (8) into Eq. (7), one can show that in the case of light-absorbing aerosol overlying cloud

$$F^{SW}_{cloudy}(\langle\tau_c\rangle) - \langle F^{SW}_{cloudy}\rangle \approx [1-T^2(\tau_a)][R^{SW}_{cloud}(\langle\tau_c\rangle) - \langle R^{SW}_{cloud}\rangle]. \tag{9}$$

Because $T^2(\tau_a) < 1$ and the term $R^{SW}_{cloud}(\langle\tau_c\rangle) - \langle R^{SW}_{cloud}\rangle > 0$, $F^{SW}_{cloudy}(\langle\tau_c\rangle) - \langle F^{SW}_{cloudy}\rangle > 0$. In other words, in the case of light-absorbing aerosol above cloud, using the grid mean COT to estimate the cloudy-sky DARF is expected to result in positive bias when cloud has significant sub-grid horizontal heterogeneity. Moreover, the bias can be expected to increase with AOT because the $T^2(\tau_a)$ decreases with AOT. Furthermore, because both $R^{SW}_{cloud}(\langle\tau_c\rangle)$ and $\langle R^{SW}_{cloud}\rangle$ increase with COT, the bias is also expected to increase with COT. Note that the above simple argument is only intended to shed some light on the qualitative behavior of the bias due to the sub-grid cloud inhomogeneity.

To test our understanding, we carried out the following numerical sensitivity study, in which we use a lognormal distribution to represent the sub-grid scale COT heterogeneity, i.e.,

$$p(\tau_c) = \frac{1}{\tau_c\sigma\sqrt{2\pi}}\exp\left[-\frac{(\ln\tau_c - \ln\tau_0)^2}{2\sigma^2}\right]. \tag{10}$$

Following [48,50] we use the cloud homogeneity index χ, defined as

$$\chi = \frac{e^{\langle \ln\tau_c\rangle}}{\langle\tau_c\rangle} = \frac{\exp\left(\int_0^\infty \ln\tau_c p(\tau_c)\,d\tau_c\right)}{\int_0^\infty \tau_c p(\tau_c)\,d\tau_c}, \tag{11}$$

as a quantitative index for sub-grid cloud heterogeneity. Note that $0 \le \chi \le 1$ and the larger the χ is, the more homogenous the cloud. For a lognormal $p(\tau_c)$, the χ has an analytical solution $\chi = e^{-\sigma^2/2}$. Using the RRTM-SW3 model, we computed two sets of instantaneous cloudy-sky TOA DARF, one based on Eq. (5) (i.e., $\langle F^{SW}_{cloudy}\rangle$) and the other based on Eq. (6) (i.e., $F^{SW}_{cloudy}(\tau_a,\langle\tau_c\rangle)$). Fig. 5 shows the differences between the two as a function of above-cloud AOT under different τ_0 and χ conditions. The absolute differences between $F^{SW}_{cloudy}(\tau_a,\langle\tau_c\rangle)$ and $\langle F^{SW}_{cloudy}\rangle$ are seen to increases with both τ_0 and above-cloud AOT, which is

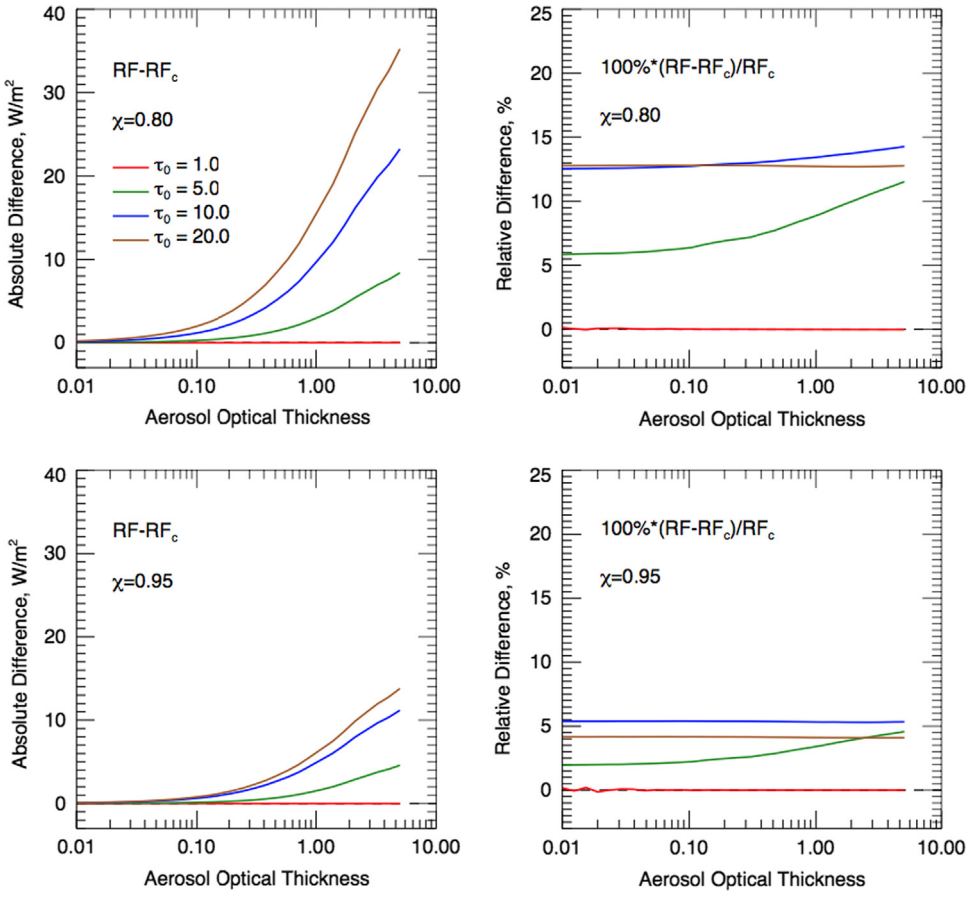

Fig. 5. Simulated absolute (left panel) and relative (right panel) differences between $F^{SW}_{cloudy}(\tau_a,\langle\tau_c\rangle)$ and $\langle F^{SW}_{cloudy}\rangle$ as a function of AOT (532 nm) for different cloud optical thickness and sub-grid cloud homogeneity index χ. In the simulation, solar zenith angle and cloud droplet effective radius are assumed to be 30° and 10 μm, respectively.

consistent with the theoretical expectation based on Eq. (9). We also note that difference in the case with smaller $\chi \approx 0.8$ (i.e., more heterogeneous cloud) is larger than that in the case with $\chi \approx 0.95$. This is also expected because the term $R^{SW}_{cloud}(\langle\tau_c\rangle) - \langle R^{SW}_{cloud}\rangle$ in Eq. (9) increases with increasing heterogeneity (i.e., decreasing χ) [48,49]. The relative difference between $F^{SW}_{cloudy}(\tau_a, \langle\tau_c\rangle)$ and $\langle F^{SW}_{cloudy}\rangle$ behaves quite differently from the absolute difference. For both optically thin $\tau_0 = 1$ and thick $\tau_0 = 20$ clouds, the relative differences remain almost constant for all above-cloud COT. In the cases where $\tau_0 = 5$ and $\tau_0 = 10$ the relative differences increase significantly with increasing above-cloud COT. In general, the absolute differences between $F^{SW}_{cloudy}(\tau_a, \langle\tau_c\rangle)$ and $\langle F^{SW}_{cloudy}\rangle$ from the numerical sensitivity test are consistent with the theoretical expectations, i.e., increase with increasing AOT, COT and cloud inhomogeneity (e.g., decreasing χ value).

As aforementioned, previous studies often use coarse resolution grid mean COT in ACA DARF computation (e.g., $5^\circ \times 5^\circ$ mean as in [15]). This is likely to introduce a positive bias depending on several factors as discussed above. The magnitude of this bias is estimated here using the collocated MODIS and CALIOP data set described in Section 2. Using the method described in Zhang et al. [35], we first use the CALIOP products to derive the AOT and the base altitude of ACA layer. Then, the ACA layer height is used in combination with MODIS COT–CTP histogram to obtain the $p(\tau_c)$ of under-aerosol clouds within a given $1^\circ \times 1^\circ$ grid box. Using the RRTM-SW model, we compute two sets of ACA DARF, i.e., $\langle F^{SW}_{cloudy}\rangle$ (blue) and $F^{SW}_{cloudy}(\tau_a, \langle\tau_c\rangle)$ (red). Note that, here each sample corresponds to a $1^\circ \times 1^\circ$ grid box with ACA present in a particular day during the time period of interest (i.e., July, August and September of 2006–2012). Fig. 6 (left panel) shows the histograms of $\langle F^{SW}_{cloudy}\rangle$ and $F^{SW}_{cloudy}(\tau_a, \langle\tau_c\rangle)$ based on MODIS COT–CTP histogram data. Fig. 6 (right panel) shows the histograms of absolute differences between $F^{SW}_{cloudy}(\tau_a, \langle\tau_c\rangle)$ and $\langle F^{SW}_{cloudy}\rangle$. Consistent with the theoretical expectations, $F^{SW}_{cloudy}(\tau_a, \langle\tau_c\rangle)$ is systematically larger than $\langle F^{SW}_{cloudy}\rangle$. On regional average, the bias is about 10%. However, the bias is a strong function of sub-grid cloud homogeneity index χ. Fig. 7 shows the relative difference between $F^{SW}_{cloudy}(\tau_a, \langle\tau_c\rangle)$ and $\langle F^{SW}_{cloudy}\rangle$ as a function of χ derived from $p(\tau_c)$ based on Eq. (11) for the samples with significant DARF (i.e., samples with absolute value of $\langle F^{SW}_{cloudy}\rangle$ larger than 0.005 W m^{-2}). Similar to previous studies [50], we found most χ values to fall between 0.5 and 1.0. Consistent with theoretical intuition, the relative difference between $F^{SW}_{cloudy}(\tau_a, \langle\tau_c\rangle)$ and $\langle F^{SW}_{cloudy}\rangle$ decreases with increasing sub-grid homogeneity from about 50% when $\chi = 0.5$ to 4% when $\chi = 0.9$. A simple fit is used to achieve a formula relating the relative

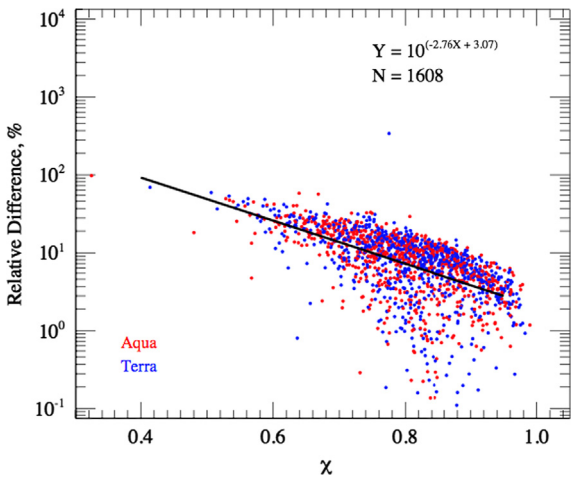

Fig. 7. Relative difference ($> 0.1\%$) $\varepsilon = (\langle F^{SW}_{cloudy}(\tau_a, \langle\tau_c\rangle) - \langle F^{SW}_{cloudy}\rangle) / \langle F^{SW}_{cloudy}\rangle) \times 100\%$ between $F^{SW}_{cloudy}(\tau_a, \langle\tau_c\rangle)$ and $\langle F^{SW}_{cloudy}\rangle$ as a function of sub-grid cloud homogeneity index, χ, computed based on Terra (blue) and Aqua (red) observations. The black solid straight line corresponds to a linear regression of $\log_{10}\varepsilon$ with respect to χ. (For interpretation of the references to color in this figure legend, the reader is referred to the web version of this article.)

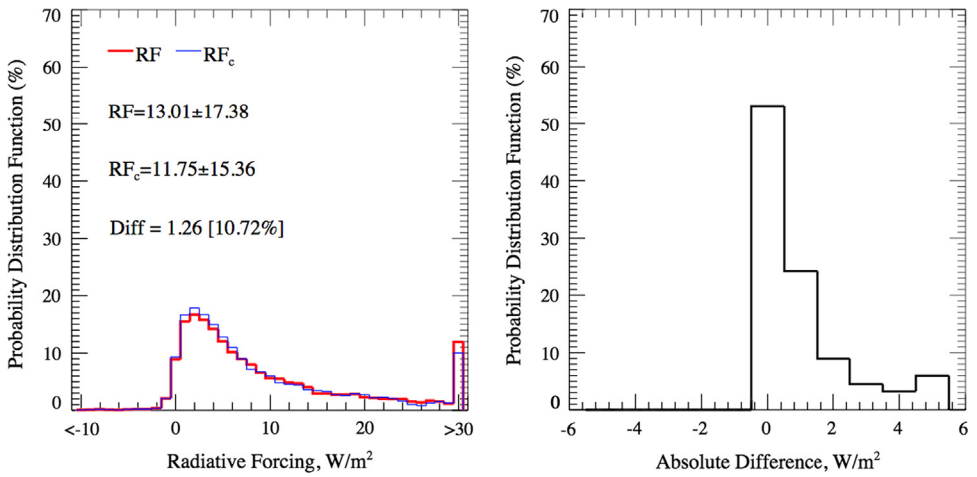

Fig. 6. (Left panel) Probability distribution functions of $F^{SW}_{cloudy}(\tau_a, \langle\tau_c\rangle)$ (red) and $\langle F^{SW}_{cloudy}\rangle$ (blue) simulated based on MODIS (Terra and Aqua combined) and CALIPSO observations. (Right panel) Probability distribution functions of the absolute difference between $F^{SW}_{cloudy}(\tau_a, \langle\tau_c\rangle)$ (red) and $\langle F^{SW}_{cloudy}\rangle$. (For interpretation of the references to color in this figure legend, the reader is referred to the web version of this article.)

difference between $F^{SW}_{cloudy}(\tau_a,\langle\tau_c\rangle)$ and $\langle F^{SW}_{cloudy}\rangle$ and χ:

$$\varepsilon = 10^{-2.76\chi+3.07}, \quad (12)$$

where $\varepsilon = (F^{SW}_{cloudy}(\tau_a,\langle\tau_c\rangle) - \langle F^{SW}_{cloudy}\rangle)/\langle F^{SW}_{cloudy}\rangle \times 100\%$. One can easily estimate the accuracy of $F^{SW}_{cloudy}(\tau_a,\langle\tau_c\rangle)$ in comparison with $\langle F^{SW}_{cloudy}\rangle$, based on the value of χ for a given grid box. For example, for a grid box with χ around 0.8, using the grid mean COT in cloudy-sky DARF computation would lead to about 7% bias. It should be noted that Eq. (12) is specific to the South-East Atlantic region considered in this study. Further investigations are needed in the future to study the impact of cloud inhomogeneity on cloudy-sky aerosol forcing in other regions and for other aerosol types.

It should also be noted that the above analysis is based on the operational CALIOP AOT retrieval, which tends to underestimate the true value according to recent studies [12,40]. We investigated the impact of this underestimation on the results shown in this section through several sensitivity tests. First, we increased the operational AOT retrieval from CALIOP by a factor of two in the light of the recent studies [12,40] and did the tests in Figs. 5–7 again. Furthermore, to investigate the impact of aerosol absorption uncertainty, we have also perturbed the single-scattering albedo of the aerosol from 0.85 to 0.8 and 0.9 in both control experiment based on the operational CALIOP AOT and double-AOT experiment (so a total of 6 tests). Qualitatively, the results from these sensitivity tests are very similar to those shown in Figs. 5–7. Quantitatively, the absolute magnitude of the bias due to sub-grid cloud inhomogeneity increases with both AOT and aerosol absorption. Interested readers are referred to Supplementary materials for details. Overall, the sensitivity tests confirm that using grid-mean COT without considering sub-grid scale cloud inhomogeneity tend to result in systematic bias in DARF computation.

5. Conclusion and discussion

In this study, we use collocated CALIOP and MODIS data to investigate the influence of cloud fraction diurnal cycle and sub-grid scale COT variability on estimating the all-sky DARF in the southeast Atlantic region. The results demonstrate that the diurnal variation of all-sky DARF is dependent on the diurnal variation of both solar zenith angle and cloud fraction. Using the instantaneous cloud fraction from polar-orbiting satellites may lead to systematic bias in all-sky DARF computation even if the diurnal variation of solar zenith angle is taken into account. Through comparison with a sinusoidal cloud fraction diurnal model, we found that assuming a constant cloud fraction in DARF computation can lead to a typical 10–20% of errors depending on whether Terra or Aqua MODIS cloud fraction is used (see Table 2). However, the error can be up to more than 50% when aerosol absorption is weak (see Table 4). Our results also indicate that due to the plane-parallel albedo bias using grid mean cloud optical thickness, i.e., ignoring sub-grid scale cloud horizontal variability, can lead to significant overestimate of the cloudy-sky (and therefore all-sky) DARF (see Figs. 5–7). This bias increases with decreasing sub-grid cloud homogeneity index χ. A simple formula $\varepsilon = 10^{-2.76\chi+3.07}$, where ε is the bias in percent, is derived based on MODIS observation to related the magnitude of the bias and χ. Several recent studies have shown that the current CALIOP operational retrieval algorithm tends to underestimate the AOT. In addition, aerosol absorption is also subject to substantial uncertainty. Our sensitivity tests confirm that these uncertainties do not affect our conclusions. Nevertheless, efforts should be made to reduce these uncertainties.

Based on these results from this study, we recommend future studies to account for both cloud diurnal cycle and sub-grid cloud variability in order to achieve most accurate estimate of all-sky DARF. The high-frequency observations from the SEVIRI instrument provide an excellent opportunity to study the cloud diurnal cycle over the southeast Atlantic region, which should be explored in future research. As demonstrated in this study and previous ones, the contrast between Terra and Aqua MODIS cloud fraction also provides an opportunity to estimate the strength of cloud diurnal cycle, which should be considered in diurnal DARF computation to avoid systematic bias. Recently, Zhang et al. [35] developed a novel method which utilizes MODIS COT–CTP joint histogram and ACA height information from CALIOP to derive the sub-grid statistics of cloud optical thickness for DARF computation. This method is computationally efficient in comparison with pixel-by-pixel method [5], and yet account for the impact of sub-grid scale cloud viability of all-sky DARF.

This study is only the first step toward a comprehensive understanding of the all-sky DARF. There are many factors to explore in the future. In this study we have ignored the diurnal variation of above-cloud aerosols. Based on AERONET observation, Eck et al. [42] noted a rather strong diurnal variation of AOT over the South Africa continent region, possibly due to a diurnal burning cycle. However, a more rent study by Arola et al. [51] based all possible AERONET sites suggested that the diurnal variation of AOT has rather smaller impact on the diurnal mean DARF. Nevertheless, the important of aerosol diurnal variation should be explored in the future. In this study, for simplicity we have also assumed that within a latitude–longitude grid-box the cloudy and clear-sky regions have the same AOT. This assumption is probably valid over the ocean because the background AOT is generally small in comparison with the transported aerosol layer above cloud. Even if the AOT over clear-sky region is larger than the above-cloud AOT, using a constant cloud fraction in all-sky DARF is still likely to be biased, although the magnitude of bias needs to be further assessed in the future.

Acknowledgments

We would like to acknowledge the Atmospheric and Environmental Research, Inc. for developing the RRTM_SW model and making it publicly available. The CALIPSO data used in this study are from the NASA Langley Distributed Active Archive Center (DAAC). The MODIS data are from the NASA Level-1 and Atmosphere Achieve and Distribution

System (LAADS). This research is supported by the faulty start-up fund to Z. Zhang from UMBC.

Appendix A. Supplementary materials

Supplementary data associated with this article can be found in the online version at http://dx.doi.org/10.1016/j.jqsrt.2014.03.014.

References

[1] Yu H, Kaufman YJ, Chin M, Feingold G, Remer LA, Anderson TL, et al. A review of measurement-based assessments of the aerosol direct radiative effect and forcing. Atmos Chem Phys 2006;6:613–66.

[2] Schulz M, Textor C, Kinne S, Balkanski Y, Bauer S, Berntsen T, et al. Radiative forcing by aerosols as derived from the AeroCom present-day and pre-industrial simulations. Atmos Chem Phys 2006;6:5225–46.

[3] Winker DM, Tackett JL, Getzewich BJ, Liu Z, Vaughan MA, Rogers RR. The global 3-D distribution of tropospheric aerosols as characterized by CALIOP. Atmos Chem Phys 2013;13:3345–61.

[4] Devasthale A, Thomas MA. A global survey of aerosol–liquid water cloud overlap based on four years of CALIPSO-CALIOP data. Atmos Chem Phys 2011;11:1143–54.

[5] Meyer K, Platnick S, Oreopoulos L, Lee D. Estimating the direct radiative effect of absorbing aerosols overlying marine boundary layer clouds in the southeast Atlantic using MODIS and CALIOP. J Geophys Res—Atmos 2013;118:1–15.

[6] Waquet F, Riedi J, Labonnote LC, Goloub P, Cairns B, Deuzé JL, et al. Aerosol remote sensing over clouds using A-train observations. J Atmosph Sci 2009;66:2468–80.

[7] Waquet F, Cornet C, Deuzé JL, Dubovik O, Ducos F, Goloub P, et al. Retrieval of aerosol microphysical and optical properties above liquid clouds from POLDER/PARASOL polarization measurements. Atmos Meas Tech 2013;6:991–1016.

[8] Torres O, Jethva H, Bhartia PK. Retrieval of aerosol optical depth above clouds from OMI observations. Sensit Anal Case Stud 2012;69:1037–53.

[9] Jethva H, Torres O, Remer LA, Bhartia PK. A color ratio method for simultaneous retrieval of aerosol and cloud optical thickness of above-cloud absorbing aerosols from passive sensors: application to MODIS measurements. IEEE Trans Geosci Remote Sens 2013;51:3862–70.

[10] Yu H, Zhang Z. New directions: emerging satellite observations of above-cloud aerosols and direct radiative forcing. Atmos Environ 2013;72:36–40.

[11] Waquet F, Peers F, Ducos F, Goloub P, Platnick S, Riedi J, et al. Global analysis of aerosol properties above clouds. Geophys Res Lett 2013;40:5809–14.

[12] Jethva H, Torres O, Waquet F, Chand D, Hu Y. How do A-train sensors intercompare in the retrieval of above-cloud aerosol optical depth? A case study-based assessment Geophys Res Lett 2014;41:186–92.

[13] Keil A, Haywood JM. Solar radiative forcing by biomass burning aerosol particles during SAFARI 2000: a case study based on measured aerosol and cloud properties. J Geophys Res 2003;108:8467.

[14] Abel SJ, Highwood EJ, Haywood JM, Stringer MA. The direct radiative effect of biomass burning aerosols over southern Africa. Atmos Chem Phys 2005;5:1999–2018.

[15] Chand D, Wood R, Anderson TL, Satheesh SK, Charlson RJ. Satellite-derived direct radiative effect of aerosols dependent on cloud cover. Nat Geosci 2009;2:181–4.

[16] Wilcox EM. Direct and semi-direct radiative forcing of smoke aerosols over clouds. Atmos Chem Phys 2011;11:20947–72 (Discussions).

[17] Wilcox EM. Stratocumulus cloud thickening beneath layers of absorbing smoke aerosol. Atmos Chem Phys 2010;10:11769–77.

[18] Oikawa E, Nakajima T, Inoue T, Winker D. A study of the shortwave direct aerosol forcing using ESSP/CALIPSO observation and GCM simulation. J Geophys Res 2013;118:3687–708.

[19] Costantino L, Bréon FM. Satellite-based estimate of aerosol direct radiative effect over the South-East Atlantic. Atmos Chem Phys 2013;13:23295–324(Discussions).

[20] Chand D, Anderson TL, Wood R, Charlson RJ, Hu Y, Liu Z, et al. Quantifying above-cloud aerosol using spaceborne lidar for improved understanding of cloudy-sky direct climate forcing. J Geophys Res 2008;113:181–4.

[21] Rozendaal MA, Leovy CB, Klein SA. An observational study of diurnal variations of marine stratiform cloud. J Clim 1995;8:1795–809.

[22] Wood R, Bretherton CS, Hartmann DL. Diurnal cycle of liquid water path over the subtropical and tropical oceans. Geophys Res Lett 2002;29:2092.

[23] Bergman JW, Salby ML. Diurnal variations of cloud cover and their relationship to climatological conditions. J Clim 1996;9:2802–20.

[24] de Graaf M, Tilstra LG, Wang P, Stammes P. Retrieval of the aerosol direct radiative effect over clouds from spaceborne spectrometry. J Geophys Res 2012;117.

[25] Di Girolamo L, Liang L, Platnick S. A global view of one-dimensional solar radiative transfer through oceanic water clouds. Geophys Res Lett 2010;37:L18809.

[26] Zhang Z, Platnick S. An assessment of differences between cloud effective particle radius retrievals for marine water clouds from three MODIS spectral bands. J Geophys Res 2011;116:D20215.

[27] Zhang Z, Ackerman AS, Feingold G, Platnick S, Pincus R, Xue H. Effects of cloud horizontal inhomogeneity and drizzle on remote sensing of cloud droplet effective radius: case studies based on large-eddy simulations. J Geophys Res 2012;117:D19208.

[28] Oreopoulos L, Cahalan RF, Platnick S. The plane-parallel albedo bias of liquid clouds from MODIS observations. J Clim 2007;20:5114–25.

[29] Cahalan RF, Joseph JH. Fractal statistics of cloud fields. Mon Weather Rev 1989;117:261–72.

[30] Platnick S, King M, Ackerman S, Menzel W, Baum B, Riedi J, et al. The MODIS cloud products: algorithms and examples from Terra. IEEE Trans Geosci Remote Sens 2003;41:459–73.

[31] Meskhidze N, Remer LA, Platnick S, Negrón Juárez R, Lichtenberger AM, Aiyyer AR. Exploring the differences in cloud properties observed by the Terra and Aqua MODIS sensors. Atmos Chem Phys 2009;9:3461–75.

[32] Hong G, Yang P, Gao B-C, Baum BA, Hu YX, King MD, et al. High cloud properties from three years of MODIS Terra and Aqua collection—4 data over the tropics. J Appl Meteorol Climatol 2007;46:1840–56.

[33] Minnis P, Sun-Mack S, Chen Y, Khaiyer MM, Yi Y, Ayers JK, et al. CERES edition-2 cloud property retrievals using TRMM VIRS and Terra and Aqua MODIS data—Part II: examples of average results and comparisons with other data. IEEE Trans Geosci Remote Sens 2011;49:4401–30.

[34] King MD, Platnick S, Menzel WP, Ackerman SA, Hubanks PA. Spatial and temporal distribution of clouds observed by MODIS onboard the Terra and Aqua satellites. IEEE Trans Geosci Remote Sens 2013;51:3826–52.

[35] Zhang Z, Meyer K, Platnick S, Oreopoulos L, Lee D, Yu H. A novel method for estimating shortwave direct radiative effect of above-cloud aerosols using CALIOP and MODIS data. Atmos Meas Tech 2013;6:9993–10020(Discussion).

[36] Schulz J, Albert P, Behr HD, Caprion D, Deneke H, Dewitte S, et al. Operational climate monitoring from space: the EUMETSAT Satellite Application Facility on Climate Monitoring (CM-SAF). Atmos Chem Phys 2009;9:1687–709.

[37] Roebeling R, Feijt A, Stammes P. Cloud property retrievals for climate monitoring: implications of differences between Spinning Enhanced Visible and Infrared Imager (SEVIRI) on METEOSAT-8 and Advanced Very High Resolution Radiometer (AVHRR) on NOAA-17. J Geophys Res 2006;111:D20210.

[38] Winker DM, Vaughan MA, Omar A, Hu Y, Powell KA, Liu Z, et al. Overview of the CALIPSO mission and CALIOP data processing algorithms. J Atmos Ocean Technol 2009;26:2310–23.

[39] Kacenelenbogen M, Vaughan MA, Redemann J, Hoff RM, Rogers RR, Ferrare RA, et al. An accuracy assessment of the CALIOP/CALIPSO version 2/version 3 daytime aerosol extinction product based on a detailed multi-sensor, multi-platform case study. Atmos Chem Phys 2011;11:3981–4000.

[40] Kacenelenbogen M, Redemann J, Vaughan MA, Omar AH, Russell PB, Burton S, et al. An evaluation of CALIOP/CALIPSO's aerosol-above-cloud (AAC) detection and retrieval capability over North America. J Geophys Res—Atmos 2013;119:230–44.

[41] Leahy LV, Anderson TL, Eck TF, Bergstrom RW. A synthesis of single scattering albedo of biomass burning aerosol over southern Africa during SAFARI 2000. Geophys Res Lett 2007;34:L12814.

[42] Eck TF, Holben BN, Ward DE, Mukelabai MM, Dubovik O, Smirnov A, et al. Variability of biomass burning aerosol optical characteristics in southern Africa during the SAFARI 2000 dry season campaign and a comparison of single scattering albedo estimates from radiometric measurements. J Geophys Res 2003;108:8477.

[43] Young SA, Vaughan MA, Kuehn RE, Winker DM. The Retrieval of profiles of particulate extinction from Cloud–Aerosol Lidar and

Infrared Pathfinder Satellite Observations (CALIPSO) Data: uncertainty and error sensitivity analyses 2013;30:395–428.
[44] Molineaux B, Ineichen P, O'Neill N. Equivalence of pyrheliometric and monochromatic aerosol optical depths at a single key wavelength. Appl Opt 1998;37:7008–18.
[45] Yu H, Zhang Y, Chin M, Liu Z, Omar A, Remer LA, et al. An integrated analysis of aerosol above clouds from A-train multi-sensor measurements. Remote Sens Environ 2012;121:125–31.
[46] Clough SA, Shephard MW, Mlawer EJ, Delamere JS, Iacono MJ, Cady-Pereira K, et al. Atmospheric radiative transfer modeling: a summary of the AER codes. J Quant Spectrosc Radiat Transf 2005;91:233–44.
[47] Iacono MJ, Mlawer EJ, Clough SA, Morcrette J-J. Impact of an improved longwave radiation model, RRTM, on the energy budget and thermodynamic properties of the NCAR community climate model, CCM3. J Geophys Res 2000;105:14873–90.
[48] Cahalan R, Ridgway W, Wiscombe W, Bell T, Snider J. The albedo of fractal stratocumulus clouds. J Atmosph Sci 1994;51:2434–55.
[49] Oreopoulos L, Davies R. Plane parallel albedo biases from satellite observations. Part I: dependence on resolution and other factors. J Clim 1998;11:919–32.
[50] Oreopoulos L, Cahalan RF. Cloud inhomogeneity from MODIS. J Clim 2005;18:5110–24.
[51] Arola A, Eck TF, Huttunen J, Lehtinen KEJ, Lindfors AV, Myhre G, et al. Influence of observed diurnal cycles of aerosol optical depth on aerosol direct radiative effect. Atmos Chem Phys 2013;13:7895–901.